

Convolutional Neural Network for Phase-Only Hologram Optimization Based on the Point Source Method With the Holographic Viewing-Window

Yun Chen^{ID}, Tianshun Zhang^{ID}, Minjie Hua^{ID}, Mingxin Zhou^{ID}, and Jianhong Wu^{ID}

Abstract—An optimization algorithm for phase-only hologram (POH) based on the point source method (PSM) with the holographic viewing-window (HVW) by using a convolutional neural network (CNN) is proposed. The network training adopts an unsupervised strategy that maps the target image to optimized constant phases (OCPs) corresponding to the wavefront of each point source instead of random constant phases (RCPs), and then the optimized POH can be obtained by wavefront superposition. The simulation and experimental results show that the speckle noise of the reconstruction is significantly suppressed compared with the initial random phase method (RPM), which demonstrates the feasibility of the proposed method and shows a strong generalization ability of the trained CNN. The HVW of a holographic near-eye display (NED) has a continuous observation range of about 6 mm in the horizontal direction without using additional optical expansion elements, and a complete high-quality image can be observed within this range.

Index Terms—Holography, convolutional neural network, point source method, holographic viewing-window.

I. INTRODUCTION

HOLOGRAPHIC display technology has been widely used in the research of augmented reality (AR) and near-eye displays (NED) in recent years [1], [2]. Since the spatial light modulator (SLM) can only modulate amplitude or phase, the encoding methods of computer-generated hologram (CGH) can be divided into amplitude-type and phase-type. The phase-type has higher diffraction efficiency without the conjugate image and the space bandwidth product (SBP) is not theoretically sacrificed, so it is very suitable for holographic display.

The essence of how to encode a phase-only hologram (POH) is an ill-posed problem, which the same purpose of different

Manuscript received 25 July 2022; accepted 27 July 2022. Date of publication 29 July 2022; date of current version 5 August 2022. This work was supported in part by the Priority Academic Program Development of Jiangsu Higher Education Institutions, and in part by The Strategic Priority Research Program of Chinese Academy of Sciences under Grant XDA25020314. (*Corresponding author: Jianhong Wu*)

The authors are with the School of Optoelectronic Science and Engineering & Collaborative Innovation Center of Suzhou Nano Science and Technology, Soochow University, Suzhou 215006, China, and also with the Key Lab of Advanced Optical Manufacturing Technologies of Jiangsu Province & Key Lab of Modern Optical Technologies of Education Ministry of China, Soochow University, Suzhou 215006, China (e-mail: 13770955370@163.com; tszhang163@163.com; mjhuas28@163.com; 1147865692@qq.com; jhwu@suda.edu.cn).

Digital Object Identifier 10.1109/JPHOT.2022.3194966

algorithms is to obtain a more optimal solution that can reconstruct high-quality images. Common optimization algorithms are mainly divided into iterative and non-iterative algorithms. Iterative algorithms mainly include the Gerchberg-Saxton (GS) algorithm [3], [4], the gradient descent algorithm [5], and the Wirtinger algorithm [6], which all take a lot of time to calculate. Non-iterative algorithms mainly have complex amplitude modulation (CAM), error diffusion [7], and so on. The commonly used CAMs are the double phase method [8]–[10] and the hologram bleaching method [11], [12], which achieve high-quality images at the expense of the SBP.

The most important step before the encoding is to calculate the wavefront of the target object, which is mainly divided into the point source method (PSM) [13], the polygon-based method [14], and the layer-based method [15]. Among them, the basic principle of the PSM is to decompose the target object into a series of self-luminous point sources, and then superimposes the wavefront of each point source on the hologram plane to obtain the wavefront information of the target object. Since the PSM can reconstruct objects with fine structures and is easy to express visual effects such as lighting and occlusion, it is widely used in holographic displays. The PSM often uses the CAM and the initial random phase method (RPM) [16], [17] to encode the wavefront. Compared with other methods, the RPM is simpler and theoretically does not sacrifice the SBP. It adds random constant phases (RCP) ($0\sim 2\pi$) to the phase of the wavefront of each point source to alleviate the distortion of the reconstructed intensity due to directly removing the amplitude of the complex field. But this method will make the reconstructed image serious speckle noise. For the optimization of POH, these constant phases are free variables that can change the phase distribution on the hologram. If suitable constant phases can be found, we may be able to obtain the optimized POH that can suppress speckle noise. These constant phases are called optimized constant phases (OCPs) in this paper.

In addition, most existing holographic NEDs used multiple viewpoints to expand eyebox to observe reconstructed images [18]–[21]. The crosstalk may occur during observation due to discontinuous viewpoints. And these works usually use additional optical expansion elements like holographic optical elements (HOEs) to generate multiple viewpoints [22], which could introduce some aberrations into these optical systems. We can actually use the characteristics of wavefront superposition

of the PSM to solve the above problems. If we can guarantee that each point of the hologram contains wavefront information of all point sources, which means that the common area of wavefront superposition is the hologram, then according to the principle of reversibility of light, the complete reconstructed image can be observed continuously and naturally within the hologram just like we look at the outside scenery through the window. The hologram that is generated by the PSM with the above feature is called holographic viewing-window (HVW) in this paper. It is obvious that for holographic NED, the HVW can be considered as the eyebox without using expansion elements. However, the holograms generated in many existing works using the PSM are composed of an array of zone plates or sub-holograms and are not the above common area [23], [24], so they can only observe the reconstructed image through the viewpoint that is usually generated by an eyepiece.

Recently, deep learning has been successfully applied to holographic displays, which can provide high-speed and high-quality image reconstruction [25], [26]. Especially for optimizing the POH, deep learning is undoubtedly a powerful tool, and a lot of interesting work has been carried out in this area [27]–[29]. These works mainly use the unsupervised strategy to train the neural network, which directly maps the target image to the phase distribution on the hologram plane by incorporating the process of numerical diffraction into the training [30]. However, these direct mapping methods are not specifically designed for the PSM, so the OPCs for each point source and the wavefront superposition on the hologram plane are not introduced in the training. In other words, that there is no unsupervised method to predict OPCs for the PSM in the existing studies.

In this paper, we proposed a novel optimization method for the POH based on the PSM with the HVW by training a CNN. The unsupervised strategy is used to train the network, which maps the target image to the OPCs ($0\sim 2\pi$) corresponding to the wavefront of each point source to obtain the optimized POH. In the simulation and experiment sections, we compare the reconstruction results by the proposed method with those by the RPM on the training set and test set, respectively, which better shows the feasibility of the proposed method and the strong generalization ability of the trained CNN. Finally, the experimental results of observing the reconstructed image with no serious speckle noise at multiple locations within the HVW are given, which provides a continuous and natural observation method for holographic NED.

II. PRINCIPLE AND METHOD

A. The Principle of the HVW

Fig. 1(a) shows the wavefront of each point source, where each wavefront is on-axis and has the same size in the x and y direction, the size of each wavefront is L_W . The process of wavefront superposition on a certain plane is shown in Fig. 1(b), where five wavefronts from a 2D target image are selected as an example to show the process. The green box is used to represent the target image and its size is L_o , the common area of the wavefront superposition is marked with a red box and its size is L_{HVW} . Note that each point of the common area contains

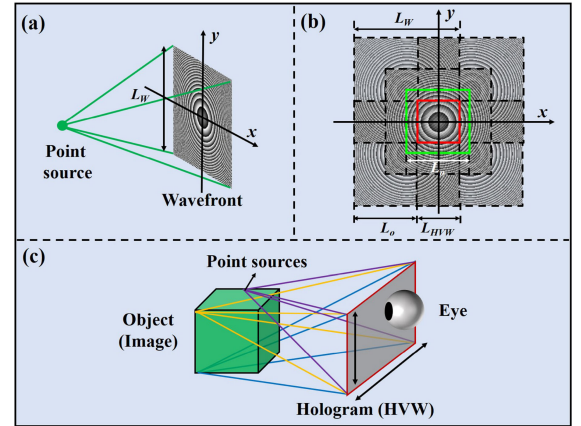


Fig. 1. The principle of the HVW. (a) The on-axis wavefront of each point source. (b) The wavefront superposition of point sources on a certain plane, where $L_W = L_o + L_{HVW}$. (c) The complete reconstructed image can be seen within the HVW from the perspective of light rays.

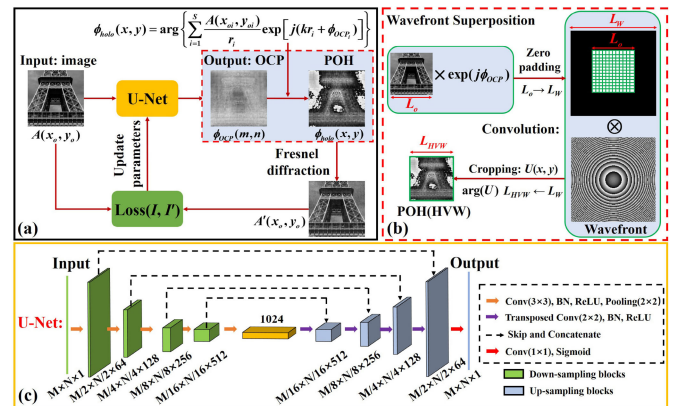


Fig. 2. The details of the training process of the CNN. (a) The training process of the network. (b) Wavefront superposition by using the convolution. (c) The structure of the U-Net model.

wavefront information of all point sources, which means that if a hologram of a target image is the above common area, a complete reconstructed image can be observed within the area. Then such a hologram is called HVW in this paper. Besides, from the above description and Fig. 1(b), it is obvious that the size of each wavefront is the sum of the size of the target image and the size of the hologram (HVW), that is, $L_W = L_o + L_{HVW}$. This relationship is a necessary condition for the existence of the HVW for the proposed method. Note that L_o can be larger than, smaller than, or equal to L_{HVW} . Moreover, the principle of the HVW can also be explained from the perspective of rays shown in Fig. 1(c), where the rays emitted from different point sources are represented by different colors. If each point of the hologram is formed by the convergence of light emitted by all point sources of the object, according to the principle of reversibility of light, a complete reconstructed image can be seen within the hologram.

B. The Details of the Training Process of the CNN

The training process of the CNN is shown in Fig. 2(a), where the input is the amplitude of the target image and the network

model adopts the U-Net that consists of five down-sampling blocks and five up-sampling blocks as shown in Fig. 2(c). Each down-sampling block consists of two convolution layers, two batch normalization layers, two activation layers (ReLU), and a pooling layer. A transposed convolution layer is added to the up-sampling block to increase the resolution and make the input and output matrices equal in size. The output layer adopts the Sigmoid function so that the output range can be easily converted to $[0, 2\pi]$. Then the output of the network is the OCP matrix that is directly mapped by the target amplitude as shown in Fig. 2(a). Note that each phase value in the OCP matrix has a one-to-one correspondence with each amplitude value in the input matrix due to the powerful ability of convolution layers to extract features. Each OCP needs to be added to the phase of the corresponding wavefront instead of the RCP [16], and then the POH can be obtained by extracting the phase after superimposing all wavefronts, which is shown in the red dotted box in Fig. 2(a). The expression of the phase distribution on the hologram plane considering the paraxial approximation is as follows:

$$\phi_{holo}(x, y) = \arg \left\{ \sum_{i=1}^S \frac{A(x_{oi}, y_{oi})}{r_i} \exp[j(kr_i + \phi_{OCP_i})] \right\} \quad (1)$$

where S is the number of point sources, $A(x_{oi}, y_{oi})$ is the amplitude of each point source, $r_i = \sqrt{(x - x_{oi})^2 + (y - y_{oi})^2 + z_i^2}$, z_i is the distance from each point source to the hologram plane, ϕ_{OCP_i} is the OCP value corresponding to each point source, k is the wave number, j is the imaginary unit, and $\arg\{\cdot\}$ is the extraction phase operation. Besides, if the complete reconstructed image can be seen within the HVW while can avoid the aliasing error on the reconstructed image plane, the distance z_i is limited by the pixel pitch of the SLM needs to satisfy the following relationship [12]:

$$z_i \geq \frac{pL_W}{\lambda} \quad (2)$$

where p is the sampling interval of the hologram, L_W is the size of the wavefront of each point source, and λ is the wavelength.

To speed up the wavefront superposition, the fast convolution method that exploits the space translation invariance of the wavefront of the point source is used to calculate the complex amplitude as shown in Fig. 2(b). To ensure the existence of the common area (HVW), here the size of the wavefront of each point source is set to be twice the size of the target image, which satisfies the condition proposed in II. A. And it also means that the size of each wavefront is twice the size of the hologram. Due to the convolution operation, the zero-padding needs to be used on the target image to make it the same size as each wavefront. Then the result of the convolution operation is cropped to a complex field $U(x, y)$ that has the same size as

the hologram. The phase distribution on the hologram of a 2D image is equivalent to (1), which the expression based on the convolution is as follows, (3) shown at the bottom of this page, where ϕ_{OCP} is the OCP matrix, \otimes represents the convolution operation, $r = \sqrt{x^2 + y^2 + z^2}$, and z is the distance between the hologram plane and the object plane, which the distance needs to satisfy (2).

Next, the reconstructed image can be obtained by numerical Fresnel diffraction of the POH as shown in Fig. 2(a). The normalized mean square error (NMSE) is used as the loss function to calculate the loss between the reconstructed intensity and the target intensity, and the loss is propagated backward to the U-Net to continuously update parameters including weights and biases, which make the training loss smaller and eventually reach a stable state during the training. Then the optimized POH can be obtained by the trained CNN. The expression of the loss function is as follows:

$$L(I, I') = \frac{1}{MN} \sum_{m=1}^M \sum_{n=1}^N [I(m, n) - \mu I'(m, n)]^2, \mu = \frac{\sum_{m=1}^M \sum_{n=1}^N I(m, n)}{\sum_{m=1}^M \sum_{n=1}^N I'(m, n)} \quad (4)$$

where I and I' are the normalized intensities of the target image and the reconstructed image, respectively, $M \times N$ is the number of point sources of the target image, and μ is a coefficient to ensure energy conservation between the target intensity and the reconstructed intensity. Compared with the MSE, the value of NMSE does not oscillate sharply and converges faster during training.

It should be pointed out that in the whole training process mentioned above, the output of the network is only the OCPs that act as free variables to change the phase distribution on the hologram, so the independence of the wavefront of each point source and the existence of the HVW will not be destroyed during multiple epochs of the training.

III. NUMERICAL SIMULATIONS

The proposed neural network is implemented in Python 3.6 based on the PyTorch 1.10.0 platform on a computer with an Intel Core i9-9900K CPU (32GB RAM), and an NVIDIA GeForce RTX 2080Ti GPU (10GB VRAM) with CUDA 11.4. We used 800 images as a training set, 100 images as a validation set, and 100 images as a test set. These target images were obtained from the DIV2K dataset [31]. Due to the limitation of GPU memory, we need to convert these target images with 2K resolution into 512×512 grayscale images by center cropping. The point source interval is $8 \mu\text{m}$, the sampling interval on the hologram is $8 \mu\text{m}$, the resolution of the hologram is 512×512 , the wavefront of each point source has 1024×1024 pixels, the wavelength is 532 nm ,

$$\phi_{holo} = \arg \left\{ \left[[A(x_o, y_o) \exp(j\phi_{OCP})]_{\substack{\text{zero-} \\ \text{padding:} \\ L_o \rightarrow L_W}} \otimes \frac{\exp(jkr)}{r} \right]_{\substack{\text{cropping:} \\ L_W \rightarrow L_{HVV}}} \right\} \quad (3)$$

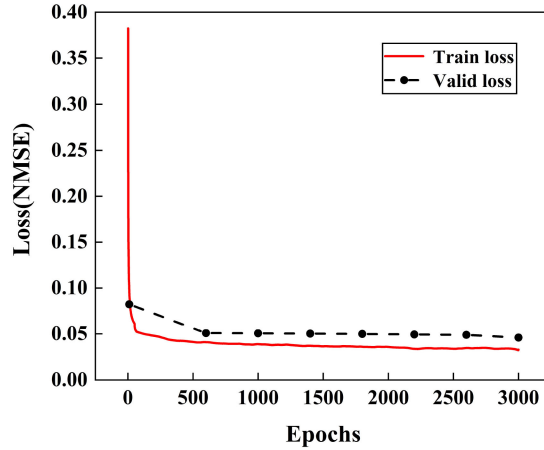


Fig. 3. The curves of loss value during the training with 3000 epochs using 800 images. The red line is the training loss and the black dotted line is the validation loss.

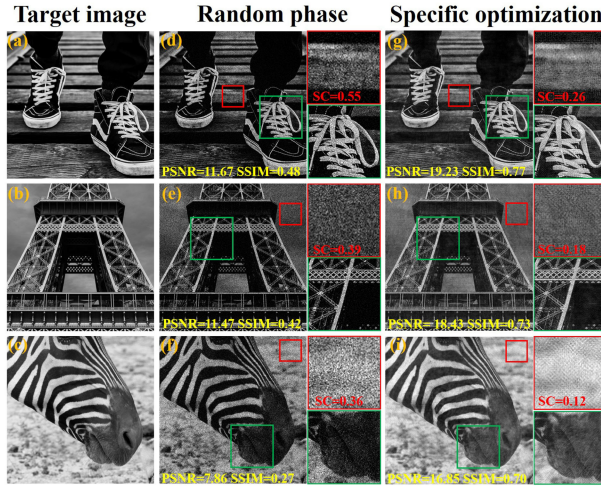


Fig. 4. Simulation results using the training set. (a)–(c) Three 512×512 target images from the training set. (d)–(f) The reconstructed images by the RPM. (g)–(i) The reconstructed images by the proposed method, which the OCPs are obtained by specific optimization based on the CNN.

and the reconstruction distance is 124 mm which satisfies (2). Taking into account the GPU performance, the batch size of the network is 4, the network parameters are updated using the Adam optimizer with a learning rate set to 0.0001, and the training period of the network is set to 3000 epochs. Fig. 3 shows the curves of the training loss and the validation loss, respectively. Due to the small batch size, the training loss oscillates slightly. The change of the loss value becomes stable after 1000 epochs, which takes about 15 h. Then an optimized POH is generated in 1.3 s, which includes the time to predict the OCPs by the trained CNN and the time to implement wavefront superposition.

Firstly, to demonstrate the feasibility that OCPs for optimizing POH and better show the great improvement in image quality after 3000 epochs training, the numerical simulation results compared with those by the RPM are shown in Fig. 4, which the three 512×512 target images are adopted from the training set. This means that the OCPs for each target image in the training set

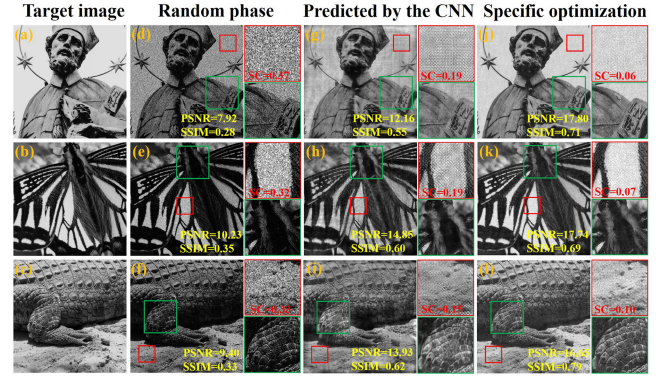


Fig. 5. Simulation results using the test set. (a)–(c) Three 512×512 target images from the test set. (d)–(f) The reconstructed images by the RPM. (g)–(i) The reconstructed images by the trained CNN. (j)–(l) The same target images are reconstructed by specific optimization.

are obtained by specific optimization instead of predicting it by the trained CNN, which the training process can be considered as an iterative optimization. Note that the peak signal-to-noise ratio (PSNR) and the structural similarity index measure (SSIM) are used to evaluate the image quality, and the speckle contrast (SC) [32] is used to measure the speckle noise. Since the SC is sensitive to the area with uneven intensity distribution, the area with uniform intensity distribution of the target image should be selected for evaluation. Compared with the results by the RPM, the PSNR of the reconstructed images by specific optimization is improved by 64.8%, 60.7%, and 114.4%, and the SSIM is improved by 60.4%, 73.8%, and 159.2%, respectively. Besides, the partial areas marked in red boxes were used to calculate SC in Fig. 4(d)–(i), and the SC of the proposed method is reduced by 52.7%, 53.8%, and 66.7% compared with the results by the RPM, respectively. For these enlarged images, the speckle noise on the reconstructed images by the proposed method is significantly suppressed. The partial areas marked with green boxes are used to demonstrate the ability to reconstruct sharper details and features.

Then, we arbitrarily select three 512×512 target images from the test set to show the generalization ability of the above trained CNN, which the corresponding OCPs are directly predicted. The numerical reconstruction results by the RPM and those by the trained CNN are given in Fig. 5(d)–(i), respectively. Compared with the RPM, the PSNR of the reconstructed images by the proposed method is improved by 53.5%, 45.2%, and 48.2%, the SSIM is improved by 96.4%, 71.4%, and 87.9%, and the SC is reduced by 48.6%, 40.6%, and 54.5%, respectively. From these partially enlarged areas in Fig. 5(g)–(i), it can be observed that even if the target images from the test set, the speckle noise on the reconstructed image is also obviously suppressed. Besides, in order to compare the results by the trained CNN with the results by specific optimization, the OCPs for the same target images in the test set can also be obtained by iterative optimization based on the CNN, which the training period is also 3000 epochs. The corresponding results are given in Fig. 5(j)–(l). Compared with those by the trained CNN, the PSNR is improved by 46.4%, 19.5%, and 19.5%, the SSIM is improved by 29.1%, 15.0%, and

TABLE I
EVALUATION OF THE PROPOSED METHOD AND THE RPM

	The average PSNR	The average SSIM
Training set (800)	17.39 dB	0.72
RPM (800)	9.41 dB	0.28
Test set (100)	14.36 dB	0.58
RPM (100)	9.65 dB	0.29

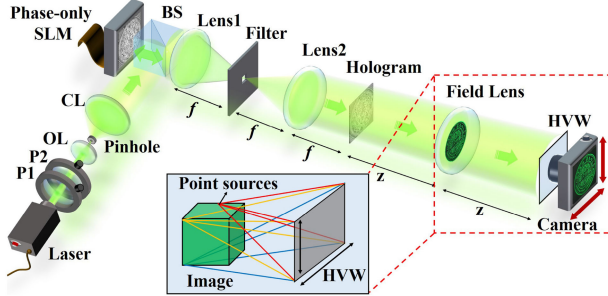


Fig. 6. The experimental setup of the holographic NED system based on the HVW.

27.4%, and the SC is reduced by 68.4%, 63.2%, and 33.3%, respectively. The above results show that the generalization ability of the trained CNN is limited compared with specific optimization.

Moreover, using the trained CNN by 800 images, the average PSNR and the average SSIM of the reconstructed images have been greatly improved compared with those of the RPM, regardless of whether the target images are from the training set or the test set, which the results are given in Table I. Compared with the RPM, the average PSNR and average SSIM on the training set are improved by 84.8% and 157.1%, respectively, while the two values are improved by 48.8% and 100% on the test set, respectively. These data again illustrate that the reconstruction results by the trained CNN are worse than those by specific optimization. Therefore, combining the above analysis of those data in Fig. 5 and Table I, there are two application directions of our proposed method as follows: 1) if we want to optimize POHs in batches and obtain higher quality reconstructed images, we can use target images as a training set, but it will take a lot of time; 2) if we want to quickly obtain the optimized POHs of target images outside the training set, we can use the trained CNN to directly predict the OCPs for the target images, but the image quality is slightly worse. Nevertheless, the structure and parameters of our neural network model need to be further optimized to improve its generalization ability.

IV. EXPERIMENTAL RESULTS

The experimental setup of the holographic NED system using the HVW to observe the reconstructed images is shown in Fig. 6. The used phase-only SLM (Holoeye Pluto VIS-016) with 1920×1080 pixels, and $8 \mu\text{m}$ pixel pitch. The experimental configuration has the same parameters as the numerical

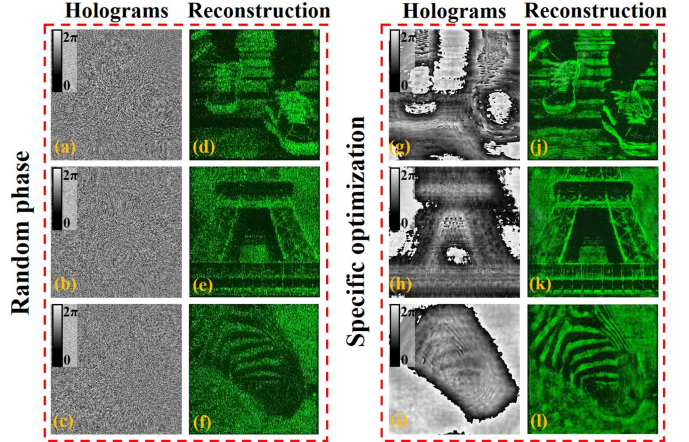


Fig. 7. Experimental results using the training set. (a)–(c) The POHs by the RPM. (d)–(f) The reconstructed images by the RPM. (g)–(i) The optimized POHs are generated by the OCPs that are obtained by specific optimization based on the CNN. (j)–(l) The reconstructed images by specific optimization.

simulation, which means that only a 512×512 area of the SLM is used to load the POH and the reconstruction distance is 124 mm. The 4f system is used to filter out the zero-order noise and translate the hologram to its back focal plane, for which a $1/4p$ carrier frequency along the y direction needs to be added to the hologram. The filter of the 4f system is a rectangular hole that has the same size as the target frequency spectrum. Since a field lens with a focal length that is half the reconstructed distance is placed on the reconstructed image plane, we can pan the hologram to the image plane of the field lens to obtain the HVW.

Firstly, the experimental results by the RPM and those by specific optimization are shown in Fig. 7, in which the used three target images from the training set are the same as in the numerical simulation. It is worth noting that these results were taken with a camera at the center of the HVW. Fig. 7(a)–(c) and (g)–(i) are the POHs generated by the RPM and the proposed method, respectively. Since the RCPs are replaced by the OCPs, the phase distributions on the hologram of the proposed method are smoother than those of the RPM, which is an important reason for suppressing speckle noise. Fig. 7(d)–(f) and (j)–(l) show the reconstructed images by the two methods. Compared with the RPM, the speckle noise of the reconstructed images by specific optimization has been significantly suppressed, so that the image quality has been greatly improved with the sharper details in visual.

Then, the experimental results using the test set are shown in Fig. 8, in which the three target images are the same as in the numerical simulation. Fig. 8(a)–(c) are the POHs generated by the RPM, Fig. 8(g)–(i) are the optimized POHs directly generated by the trained CNN, and Fig. 8(m)–(o) are the optimized POHs generated by specific optimization. The phase distributions of the optimized POHs are also smoother than those of the RPM and the optimized POHs by specific optimization have richer structures compared with those by the trained CNN. Moreover, the reconstructed images by the trained CNN and those by specific optimization are shown in Fig. 8(j)–(l) and (p)–(r), respectively,

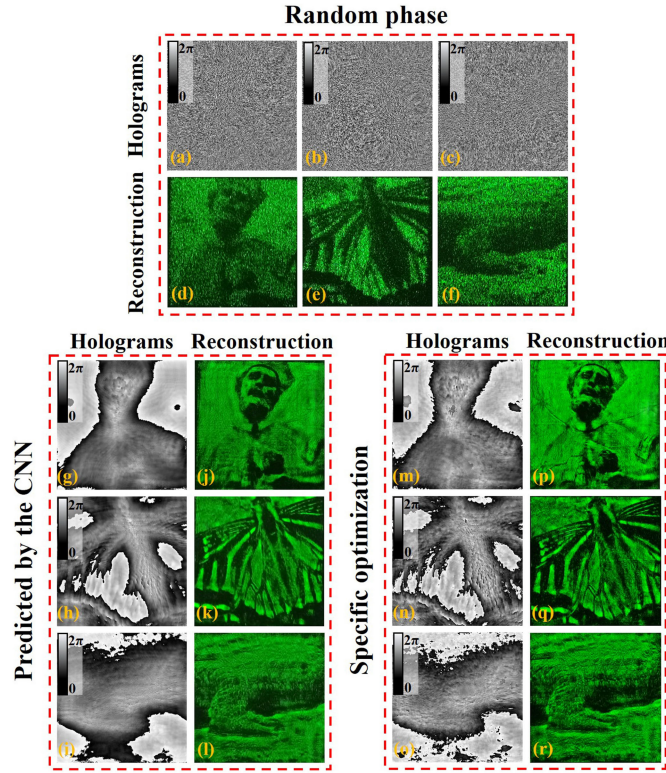


Fig. 8. Experimental results using the test set. (a)-(c) The POHs by the RPM. (d)-(f) The reconstructed images by the RPM. (g)-(i) The optimized POHs are generated by the OCPs that are predicted by the trained CNN. (j)-(l) The reconstructed images by the trained CNN. (m)-(o) The optimized POHs are generated by the OCPs that are obtained by specific optimization. (p)-(r) The reconstructed images by specific optimization.

where the speckle noise is also obviously suppressed compared with the results of the RPM in Fig. 8(d)–(f). The above results show that the trained CNN has a strong generalization ability, which the optimized POHs can reconstruct high-quality images without serious speckle noise. Meanwhile, it can be clearly observed that the reconstructed images have higher quality by specific optimization, which the details are reconstructed more finely.

Finally, the experimental results of the holographic NED by using the HVW to observe the reconstructed images are shown in Fig. 9. The experimental setup is still the optical system shown in Fig. 6. We used the proposed method to generate the optimized POH of the 512×512 target image “school badge”. Since the pixel pitch of the SLM is $8 \mu\text{m}$, the size of the HVW is about $4 \text{ mm} \times 4 \text{ mm}$. Fig. 9(b)–(d) are the observation results taken by the camera at the leftmost side, the center, and the rightmost side of the HVW, respectively. As the camera moves, the two reference objects “toy doll” move relative to the camera, but the complete “school badge” can still be observed, which verifies the feasibility of the HVW. Compared with the observation based on viewpoints, the HVW has a continuous observation range and a natural visual experience without using additional optical expansion elements. Since the camera lens has a certain aperture that is similar to the pupil, the actual observation range is slightly larger. In the experiment, the camera can move about

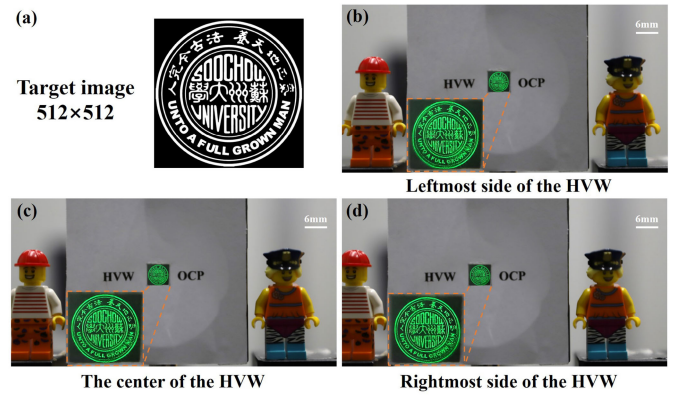


Fig. 9. The experimental results of the holographic NED by using the HVW to observe the image. The target image is the school badge of Soochow University. (a) The 512×512 target image is the school badge of Soochow University. (b) The camera is at the leftmost side of the HVW. (c) The camera is at the center of the HVW. (d) The camera is at the rightmost side of the HVW.

6 mm in the horizontal direction. It should be noted that a $1/4p$ carrier frequency along the y direction is added to the hologram to separate the target frequency spectrum from the zero-order noise, so that the HVW loses half of the observation range in the vertical direction.

V. CONCLUSION

To the best of our knowledge, this is the first study to optimize the POH based on the PSM by using the OCPs. The CNN is trained by unsupervised learning to output the OCPs corresponding to each point source, which can obtain the optimized POH to reconstruct the high-quality image without serious speckle noise. We demonstrate the feasibility of the proposed method and show a strong generalization ability of the trained CNN by simulations and experiments, which the reconstruction results compared with those by the RPM. Then according to the reconstruction results by the trained CNN and those by specific optimization, the two application directions of our proposed method are pointed out, respectively. In addition, since the wavefront superposition ensures the existence of the HVW, so a continuous observation range of about 6 mm in the horizontal direction can be obtained, and the observation method will have great application prospects in the holographic NED. The size of the reconstructed image is currently relatively small due to the limitation of the SBP. In the future, multiple SLMs will be spliced together to obtain a large-scale reconstructed image while ensuring the existence of the HVW. Moreover, the proposed method will be generalized to optimize the POHs of 3D images by designing an appropriate loss function.

REFERENCES

- [1] C. Chang, K. Bang, G. Wetzstein, B. Lee, and L. Gao, “Toward the next-generation VR/AR optics: A review of holographic near-eye displays from a human-centric perspective,” *Optica*, vol. 7, no. 11, pp. 1563–1578, 2020.
- [2] C. Chen, M. He, J. Wang, K. Chang, and Q. Wang, “Generation of phase-only holograms based on aliasing reuse and application in holographic see-through display system,” *IEEE Photon. J.*, vol. 11, no. 3, Jun. 2019, Art. no. 7000711.

- [3] R. W. Gerchberg and W. O. Saxton, "A practical algorithm for the determination of phase from image and diffraction plane pictures," *Optik*, vol. 35, no. 2, pp. 237–246, 1972.
- [4] Y. Zhao, L. Cao, H. Zhang, D. Kong, and G. Jin, "Accurate calculation of computer-generated holograms using angular-spectrum layer-oriented method," *Opt. Exp.*, vol. 23, no. 20, pp. 25440–25449, 2015.
- [5] J. Zhang, N. Pégard, J. Zhong, H. Adesnik, and L. Waller, "3D computer-generated holography by non-convex optimization," *Optica*, vol. 4, no. 10, pp. 1306–1313, 2017.
- [6] P. Chakravarthula, Y. Peng, J. Kollin, H. Fuchs, and F. Heide, "Wirtinger holography for near-eye displays," *ACM Trans. Graph.*, vol. 38, no. 6, pp. 1–13, 2019.
- [7] P. W. M. Tsang and T. C. Poon, "Novel method for converting digital Fresnel hologram to phase-only hologram based on bidirectional error diffusion," *Opt. Exp.*, vol. 21, no. 20, pp. 23680–23686, 2013.
- [8] O. Mendoza-Yero, G. Minguez-Vega, and J. Lancis, "Encoding complex fields by using a phase-only optical element," *Opt. Lett.*, vol. 39, no. 7, pp. 1740–1743, 2014.
- [9] Q. Gao, J. Liu, X. Duan, T. Zhao, X. Li, and P. Liu, "Compact see-through 3D head-mounted display based on wavefront modulation with holographic grating filter," *Opt. Exp.*, vol. 25, no. 7, pp. 8412–8424, 2017.
- [10] X. Sui, Z. He, G. Jin, D. Chu, and L. Cao, "Band-limited double-phase method for enhancing image sharpness in complex modulated computer-generated holograms," *Opt. Exp.*, vol. 29, no. 2, pp. 2597–2612, 2021.
- [11] X. Li, J. Liu, J. Jia, Y. Pan, and Y. Wang, "3D dynamic holographic display by modulating complex amplitude experimentally," *Opt. Exp.*, vol. 21, no. 18, pp. 20577–20587, 2013.
- [12] Y. Chen, M. Hua, T. Zhang, M. Zhou, J. Wu, and W. Zou, "Holographic near-eye display based on complex amplitude modulation with band-limited zone plates," *Opt. Exp.*, vol. 29, no. 14, pp. 22749–22760, 2021.
- [13] H. Zhang, N. Collings, J. Chen, B. Crossland, D. Chu, and J. Xie, "Full parallax three-dimensional display with occlusion effect using computer generated hologram," *Opt. Eng.*, vol. 50, no. 7, 2011, Art. no. 074003.
- [14] W. Lee, D. Im, J. Paek, J. Hahn, and H. Kim, "Semi-analytic texturing algorithm for polygon computer-generated holograms," *Opt. Exp.*, vol. 22, no. 25, pp. 31180–31191, 2014.
- [15] J.-S. Chen and D. P. Chu, "Improved layer-based method for rapid hologram generation and real-time interactive holographic display applications," *Opt. Exp.*, vol. 23, no. 14, pp. 18143–18155, 2015.
- [16] J. Jia et al., "Reducing the memory usage for effective computer-generated hologram calculation using compressed look-up table in full-color holographic display," *Appl. Opt.*, vol. 52, no. 7, pp. 1404–1412, 2013.
- [17] J. Jia, J. Liu, G. Jin, and Y. Wang, "Fast and effective occlusion culling for 3D holographic displays by inverse orthographic projection with low angular sampling," *Appl. Opt.*, vol. 53, no. 27, pp. 6287–6293, 2014.
- [18] S.-B. Kim and J.-H. Park, "Optical see-through Maxwellian near-to-eye display with an enlarged eyebox," *Opt. Lett.*, vol. 43, no. 4, pp. 767–770, 2018.
- [19] Z. Wang et al., "Lensless full-color holographic Maxwellian near-eye display with a horizontal eyebox expansion," *Opt. Lett.*, vol. 46, no. 17, pp. 4112–4115, 2021.
- [20] C. Jang, K. Bang, G. Li, and B. Lee, "Holographic near-eye display with expanded eye-box," *ACM Trans. Graph.*, vol. 37, no. 6, pp. 1–14, 2018.
- [21] Y. Su et al., "Projection-type multiview holographic three-dimensional display using a single spatial light modulator and a directional diffractive device," *IEEE Photon. J.*, vol. 10, no. 5, Oct. 2018, Art. no. 7000512.
- [22] X. Duan, J. Liu, X. Shi, Z. Zhang, and J. Xiao, "Full-color see-through near-eye holographic display with 80° field of view and an expanded eyebox," *Opt. Exp.*, vol. 28, no. 21, pp. 31316–31329, 2020.
- [23] T. Kurihara and Y. Takaki, "Speckle-free, shaded 3D images produced by computer-generated holography," *Opt. Exp.*, vol. 21, no. 4, pp. 4044–4054, 2013.
- [24] A. Maimone, A. Georgiou, and J. S. Kollin, "Holographic near-eye displays for virtual and augmented reality," *ACM Trans. Graph.*, vol. 36, no. 4, pp. 1–16, 2017.
- [25] L. Shi, B. Li, C. Kim, P. Kellnhofer, and W. Matusik, "Towards real-time photorealistic 3D holography with deep neural networks," *Nature*, vol. 591, no. 7849, pp. 234–239, 2021.
- [26] Y. Peng, S. Choi, N. Padmanaban, and G. Wetzstein, "Neural holography with camera-in-the-loop training," *ACM Trans. Graph.*, vol. 39, no. 6, pp. 1–14, 2020.
- [27] J. Wu, K. Liu, X. Sui, and L. Cao, "High-speed computer-generated holography using an autoencoder-based deep neural network," *Opt. Lett.*, vol. 46, no. 12, pp. 2908–2911, 2021.
- [28] H. Zheng, J. Hu, C. Zhou, and X. Wang, "Computing 3D phase-type holograms based on deep learning method," *Photonics*, vol. 8, no. 7, 2021, Art. no. 280.
- [29] M. Hossein Eypbosh, N. W. Caira, M. Atisa, P. Chakravarthula, and N. C. Pégard, "DeepCGH: 3D computer-generated holography using deep learning," *Opt. Exp.*, vol. 28, no. 18, pp. 26636–26650, 2020.
- [30] X. Sun et al., "Dual-task convolutional neural network based on the combination of the U-Net and a diffraction propagation model for phase hologram design with suppressed speckle noise," *Opt. Exp.*, vol. 30, no. 2, pp. 2646–2658, 2022.
- [31] E. Agustsson and R. Timofte, "NTIRE 2017 challenge on single image super-resolution: Dataset and study," in *Proc. IEEE Conf. Comput. Vis. Pattern Recognit. Workshops*, 2017, pp. 126–135.
- [32] D. Pi, J. Liu, and S. Yu, "Speckleless color dynamic three-dimensional holographic display based on complex amplitude modulation," *Appl. Opt.*, vol. 60, no. 25, pp. 7844–7848, 2021.